

www.acsnano.org

# Stationary Oxygen Vacancy Construction toward a Superior-Performance Ultrahigh Nickel Single-Crystal Cathode

Yongzhi Liang, Haoyu Xue, Minzhi Zhan, Hongbin Cao, Zhongxing Xu, Tongchao Liu, Xinghan Chen, Jiajie Liu, Shunning Li, Feng Pan,\* and Xinghua Tan\*



Downloaded via UNIV TOWN OF SHENZHEN on November 18, 2025 at 06:57:39 (UTC). See https://pubs.acs.org/sharingguidelines for options on how to legitimately share published articles.

Cite This: ACS Nano 2025, 19, 25879-25889



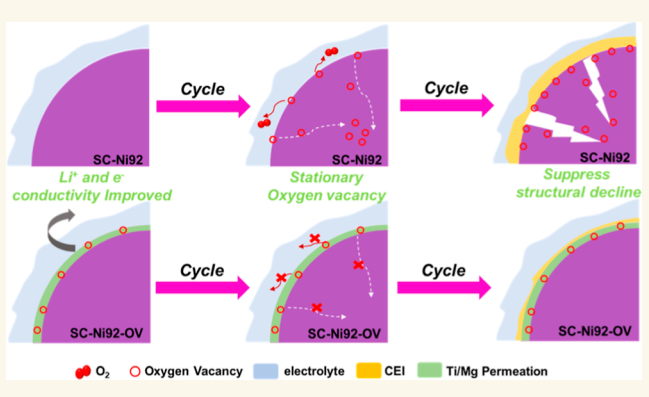
**ACCESS** I

Metrics & More

Article Recommendations

Supporting Information

ABSTRACT: Oxygen vacancies exert a complex and profound influence on the layered cathodes, especially those with ultrahigh nickel content. They can facilitate lithium-ion transport and enhance electronic conductivity, while aggressive oxygen vacancy formation causes structural degradation and electrolyte decomposition. Herein, taking ultrahigh nickel single-crystal  $LiNi_{0.92}Co_{0.06}Mn_{0.02}O_2$  (SC-Ni92) as a model material, we propose a pinning strategy to harness the benefits of oxygen vacancies while mitigating their detrimental effects. Through a carefully controlled thermal process, both oxygen vacancies and pinning atoms are successfully introduced into the surface region. The resulting anchored oxygen vacancies, capitalizing on their inherent advantages, improve conductivity



and lithium-ion diffusion. Simultaneously, the neighboring pinning atoms effectively increase the migration barrier and suppress the adverse effects of these vacancies, including electrolyte decomposition and structural degradation during longterm electrochemical cycling. Consequently, oxygen vacancy-anchored single-crystal LiNi<sub>0.92</sub>Co<sub>0.06</sub>Mn<sub>0.02</sub>O<sub>2</sub> (SC-Ni92-OV) demonstrates significantly improved high-voltage electrochemical performance, with 86.16% capacity retention after 200 cycles at 4.6 V and 1 C in a half-cell and 90.71% after 300 cycles at 4.5 V and 1 C in a full cell. This study not only provides valuable insights into the chemistry of oxygen vacancy but also introduces a viable strategy for leveraging oxygen vacancies to achieve stable high-voltage performance in ultrahigh nickel single-crystal cathodes.

KEYWORDS: oxygen vacancies, ultrahigh nickel single crystal, pinning effect, high voltage, element permeation

#### INTRODUCTION

Lithium-ion batteries (LIBs), as one of the most efficient and portable energy storage systems, are widely utilized in our daily lives. However, they still fail to meet the growing demand for electric vehicles (EVs) and consumer electronics. 1,2 Therefore, to satisfy the demands of modern society, high-voltage and high-capacity batteries with enhanced energy density and extended lifespan are urgently required.<sup>3</sup> As a key component of LIBs, the cathode not only dictates the energy density but also constitutes the largest portion of the cost. Among cathode materials, ultrahigh nickel single-crystal layered oxides (Ni content >90%) are particularly well suited to fulfill the requirements of high energy density and low cost, positioning them as promising candidates for the next generation of lithium batteries.4-6 However, operating ultrahigh nickel layered oxides at elevated voltages leads to rapid capacity fade and poor thermal stability due to lattice oxygen oxidation

and surface release.<sup>7-9</sup> The persistent and excessive evolution of oxygen species (O2, O2-, and O-) not only promotes structural degradation through the migration of newly formed oxygen vacancies (OVs) but also accelerates electrolyte decomposition due to the liberation of oxygen species. Specifically, during electrochemical processes or thermal driving, 10,11 OVs continuously form on the surface, migrate to the bulk, and then aggregate, reducing the migration barrier of transition metal atoms, 12 thereby facilitating the formation of dislocations, slip bands, and even cracks. 13 Moreover,

Received: March 31, 2025 Revised: June 3, 2025 Accepted: June 3, 2025 Published: July 10, 2025





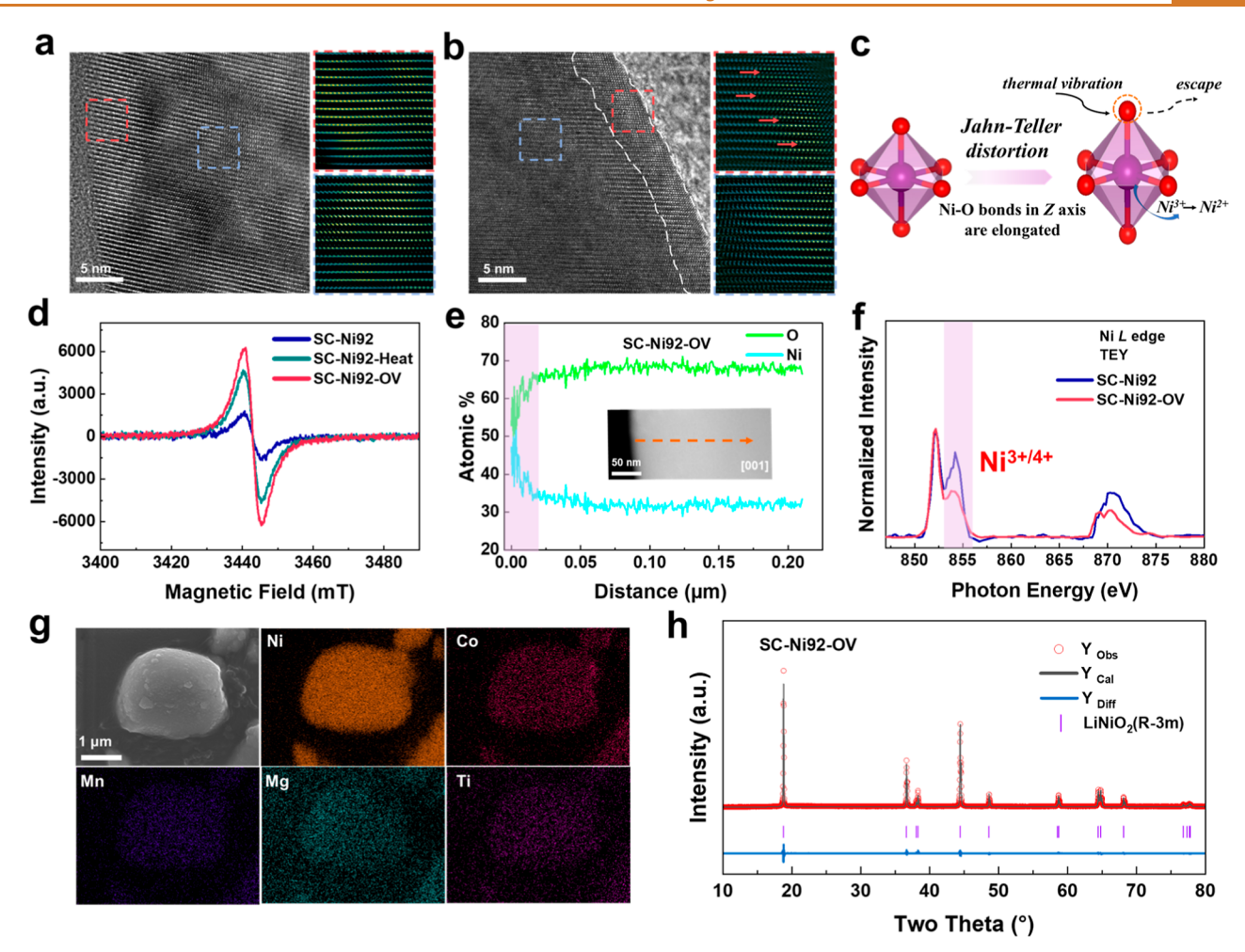


Figure 1. HRTEM images of SC-Ni92 (a) and SC-Ni92-OV (b); schematic diagrams illustrating the formation of OVs influenced by Jahn-Teller distortion upon thermal vibrations (c); electron paramagnetic resonance (EPR) profiles of SC-Ni92, SC-Ni92-Heat, and SC-Ni92-OV (d); relative content changes of O and Ni atoms in SC-Ni92-OV during the EDS line scan (e), with the inset image illustrating the corresponding line scan path; Ni L-edge s-XAS spectra using the TEY model for SC-Ni92 and SC-Ni92-OV (f); EDS mapping of Ni, Co, Mn, Mg, and Ti in SC-Ni92-OV (g); XRD pattern and the corresponding Rietveld refinement for SC-Ni92-OV (h).

liberated oxygen species oxidize the electrolyte, resulting in the formation of a high-impedance cathode electrolyte interphase (CEI) and potentially triggering thermal runaway events. <sup>14</sup> Therefore, inhibiting the continuous release of oxygen species is crucial to the successful application of ultrahigh nickel cathodes at high voltages.

Although excessive OV formation in the cathode during electrochemical operation is detrimental to battery performance, recent studies have demonstrated that OVs, classified as a type of Schottky defect in layered oxides, can enhance electrochemical performance. The introduction of OVs has been recognized as an effective strategy for improving electrochemical reaction kinetics, as OVs act as electron donors increasing electron concentration and enhancing Li<sup>+</sup> diffusion by lowering the energy barrier for Li<sup>+</sup> migration through tetrahedral sites. Likewise, OVs are a double-edged sword to ultrahigh nickel layered oxides. This paradox underscores the need for a thorough investigation into the effective utilization of OVs to optimize their benefits while minimizing the adverse effects.

Metal oxides tend to lose lattice oxygen when heated in a reductive or inert atmosphere. However, the formation of OVs at moderately high temperatures in pure oxygen is often overlooked. It has been shown that Jahn–Teller distortion

occurs spontaneously in Ni<sup>3+</sup>,<sup>20,21</sup> leading to elongation of the Ni–O bond along the Z axis and decreasing covalency. In layered structures primarily composed of Ni–O polyhedrons, oxygen is easily released, accompanied by Ni<sup>3+</sup> reduction, due to its lower reduction energy barrier (0.5–1.5 eV), compared to Co–O polyhedrons (1.8–2.7 eV).<sup>22</sup> This unstable Ni–O bond causes oxygen atoms to escape upon thermal disturbance.<sup>21</sup> From a dynamic perspective, in the reversible reaction,

$$\text{LiNiO}_2 \rightleftharpoons \text{LiNi}_{1-2x}^{3+} \text{Ni}_{2x}^{2+} \text{O}_{2-x} + \frac{x}{2} \text{O}_2$$

OV formation from oxygen loss seems to be difficult in an oxygen-rich environment. For high nickel cathode materials,  $\mathrm{Ni^{2^+}}$  reoxidation to  $\mathrm{Ni^{3^+}}$  requires a higher temperature ( $\geq 700\,^{\circ}\mathrm{C}$ ), which cannot occur at moderately high temperatures (300–500 °C) from a thermodynamic perspective. Therefore, once oxygen loss occurs due to the unstable Ni–O bonds, repair becomes difficult at moderately high temperatures. In addition, interfacial lattice strain during the surface modification process can also drive the formation of OVs, <sup>24</sup> enhancing lithium-ion transport kinetics, which had also been overlooked previously.

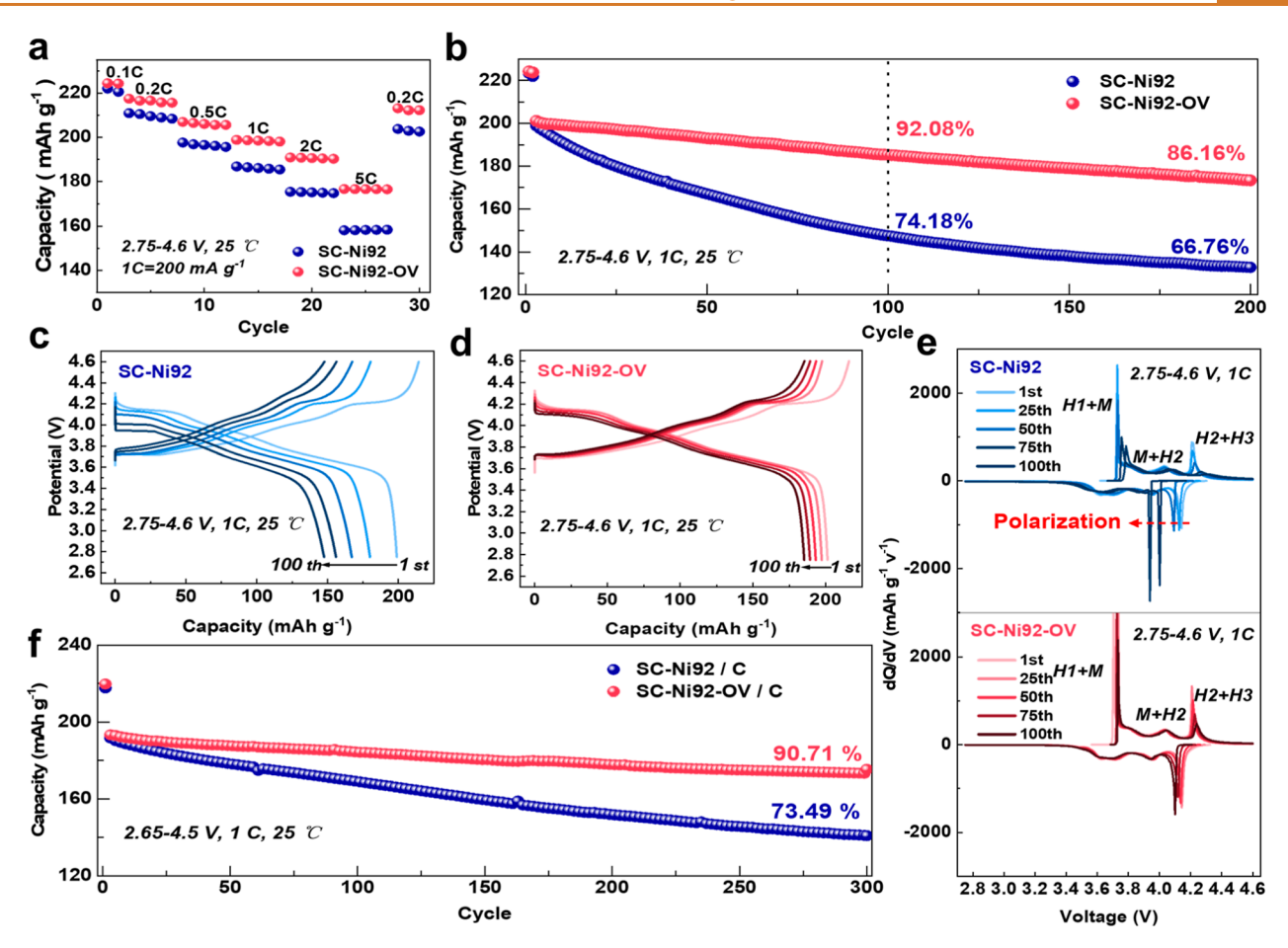


Figure 2. Rate performance (a) and 1 C cycling performance (b) of SC-Ni92 and SC-Ni92-OV within the voltage range of 2.75–4.6 V; charge/discharge curves at different cycles for SC-Ni92 (c) and SC-Ni92-OV (d), respectively; the corresponding dQ/dV curves for SC-Ni92 and SC-Ni92-OV (e); cycling performance of the two samples in full cells (f).

Herein, we introduce OVs into the near-surface region of single-crystal LiNi<sub>0.92</sub>Co<sub>0.06</sub>Mn<sub>0.02</sub>O<sub>2</sub> by exploiting the Jahn-Teller distortion-induced instability of the Ni-O bond and the difficulty of reoxidizing Ni<sup>2+</sup> at moderately high temperatures. Meanwhile, moderately high temperatures and a pure oxygen atmosphere can prevent excessive lattice oxygen loss as observed in inert or reductive atmospheres. Specifically, adequate surface OVs are constructed when the material is exposed to an oxygen atmosphere at 400 °C for 5 h, as demonstrated by electron paramagnetic resonance (EPR), energy-dispersive spectrometry (EDS), soft X-ray absorption spectroscopy (sXAS), and so on. Moreover, we present a precise pinning strategy for OVs using titanium (Ti) and magnesium (Mg) as pinning atoms, which not only promotes the formation of OVs during the heating process but also significantly inhibits structural degradation caused by excessive formation and subsequent migration of OVs to the bulk during high-voltage cycling. The preformed OVs were anchored by the Ti- and Mg-permeated layer through increasing the formation energy and the migration barrier of OVs, thereby blocking their flow network. Therefore, these stationary OVs enhance Li<sup>+</sup> and electron conductivity, suppress excessive evolution of oxygen species, and mitigate subsequent electrolyte decomposition and impedance increase. This study provides a deeper understanding of oxygen deficiency chemistry and introduces a practical strategy to stabilize

oxygen vacancies, paving the way for durable high-voltage performance in ultrahigh nickel single-crystal cathodes.

# **RESULTS**

Fabrication and Anchoring of Oxygen Vacancies. High-resolution transmission electron microscopy (HRTEM) images (Figures 1a and S1b) reveal that both the interface and the bulk of SC-Ni92 maintained a well-layered structure. The SC-Ni92 particles exhibited an intact morphology without cracks or dislocations, as observed in the transmission electron microscopy (TEM) image (Figure S1a). Its surface morphology and elemental composition are shown in Figure S2 and Table S1, respectively. As shown in Figure 1b, a 3-5 nm reconstructed layer was observed on the surface of SC-Ni92-OV, likely caused by OV formation and Ti and Mg permeation. To investigate the mechanism of OV formation, we compared the surface properties of SC-Ni92, Li-Ni<sub>0.92</sub>Co<sub>0.06</sub>Mn<sub>0.02</sub>O<sub>2</sub> heated in an oxygen atmosphere (SC-Ni92-Heat), and SC-Ni92-OV. As shown in Figure 1c, Ni<sup>3+</sup> exhibits spontaneous Jahn-Teller distortion, 21 increasing the Ni-O bond length along the Z-axis and reducing covalency. The O atom becomes highly susceptible to vibration upon exposure to thermal radiation, displacing it from its equilibrium position and forming OVs, which are accompanied by the reduction of Ni<sup>3+</sup> to Ni<sup>2+</sup>.

Electron paramagnetic resonance (EPR) was employed to qualitatively reveal OVs. 25,26 As shown in Figure 1d, the OV

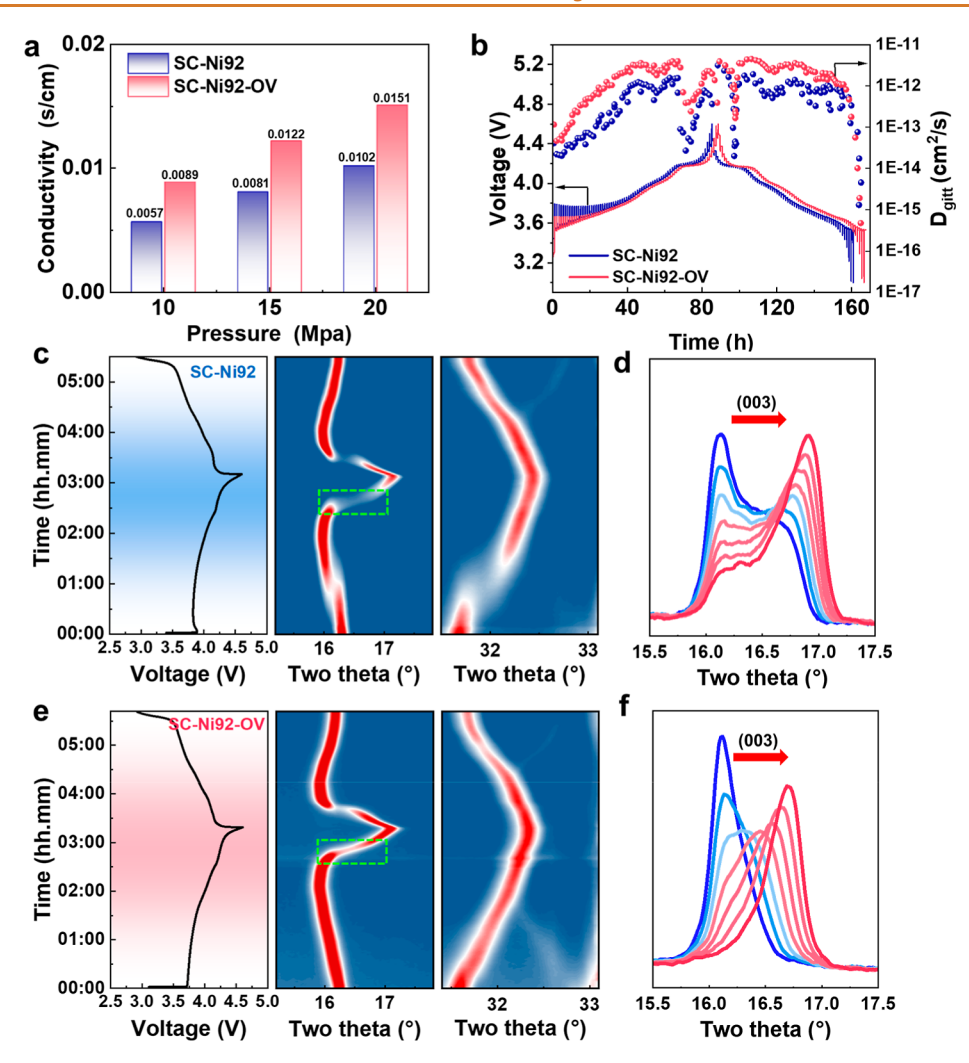


Figure 3. Electrical conductivity of SC-Ni92 and SC-Ni92-OV (a); voltage—time profiles of GITT and the Li<sup>+</sup> diffusion coefficient for SC-Ni92 and SC-Ni92-OV (b); in situ XRD characterizations of SC-Ni92 (c) and SC-Ni92-OV (e) during the initial charge/discharge process at 0.33 C; the evolution of the (003) peak (d) and (f) within the charging process range indicated by the green dotted boxes in (c) and (e).

signal strengths of SC-Ni92-OV and SC-Ni92-Heat are significantly higher than those of SC-Ni92. Furthermore, SC-Ni92-OV and SC-Ni92-Heat exhibited an oxygen-poor state near the surface, as revealed by energy-dispersive X-ray spectroscopy (EDS) line scan results (Figures 1e and S3). We further studied the interfacial chemical valence of Ni by the soft X-ray absorption spectroscopy (s-XAS) in total electron yield (TEY) mode.<sup>3,27</sup> As shown in Figure 1f, the Ni<sup>3+/4+</sup>peak of SC-Ni92-OV is significantly lower than that of SC-Ni92, corroborating the presence of more OVs near the surface of SC-Ni92-OV to maintain an overall charge balance. X-ray photoelectron spectroscopy (XPS) results further demonstrated that the Ni<sup>3+</sup>/Ni<sup>2+</sup> ratio of SC-Ni92-OV is lower than that of SC-Ni92 (Figure S4). These results demonstrate that interfacial OVs can be introduced through sintering at moderately high temperatures, even in an oxygen atmosphere.<sup>28</sup> EDS mapping (Figure 1g) revealed that Ti and Mg are uniformly distributed on the particle surfaces. Rietveld refinements of X-ray diffraction (XRD) patterns indicated that both SC-Ni92 and SC-Ni92-OV exhibited a pure hexagonal  $\alpha$ -NaFeO<sub>2</sub> structure with the R3m space group (Figures 1h and S5), and the refined results are listed in Table S2. The lattice parameters of both samples were quite similar. Moreover, when testing the Ni and O states using s-XAS in

total fluorescence yield (TFY) mode (Figure S6), which probes deeper into the bulk compared to the TEY mode, there was almost no difference between the two samples. These results suggested that OVs and Ti and Mg were limited to the near-surface region and did not significantly alter the crystal structure of the bulk phase. In brief, we successfully introduced and anchored OVs in the near-surface region of ultrahigh nickel single-crystal material through annealing and Ti and Mg permeation.

**Electrochemical Performance.** To analyze the effect of anchored OVs on the electrochemical performance of Ni92, the cycling and rate performances of SC-Ni92 and SC-Ni92-OV were tested. SC-Ni92 and SC-Ni92-OV exhibited similar initial discharge specific capacities of 224.6 mA h g<sup>-1</sup> at 0.1 C (1 C = 200 mA g<sup>-1</sup>) (Figure 2a). SC-Ni92-OV retained a specific capacity of 176.6 mA h g<sup>-1</sup> at 5 C, which was higher than that of SC-Ni92 (158.2 mA h g<sup>-1</sup>). SC-Ni92-OV displayed a capacity retention of 86.16% after 200 cycles at 1 C with a cutoff voltage of 4.6 V, significantly higher than SC-Ni92 (66.76%) (Figure 2b). Notably, SC-Ni92-OV demonstrated superior cycling performance at 4.6 V compared to other ultrahigh nickel single-crystal materials with similar nickel content (Table S3). The charge/discharge curves of SC-Ni92 and SC-Ni92-OV at different cycles are shown in Figure

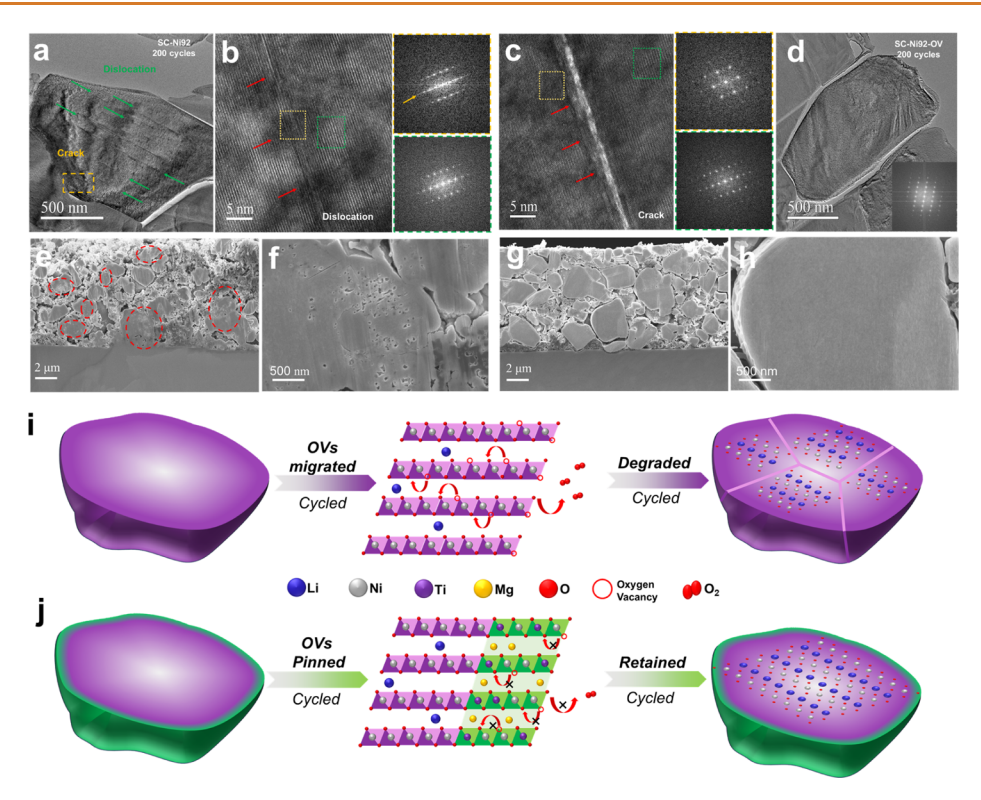


Figure 4. TEM and HRTEM images of SC-Ni92 after 200 cycles (a-c); TEM and HRTEM images of SC-Ni92-OV after 200 cycles (d); cross-sectional SEM images of delithiated SC-Ni92 (e,f) and SC-Ni92-OV (g,h) after heating at 400 °C for 4 h in an argon atmosphere; schematic diagrams of the degradation process induced by the migration of OVs (i) and the anchoring effect of Ti and Mg on OVs (j).

2c-d, where SC-Ni92-OV experienced significantly less voltage decay during cycling. As presented in Figure 2e, the corresponding differential capacity (dQ/dV) profiles show that SC-Ni92-OV exhibited better H2-H3 phase transition reversibility compared to SC-Ni92 within the voltage range 2.75-4.6 V. The H3-H2 peak shift of SC-Ni92-OV was 0.0426 V after 100 cycles, significantly lower than the 0.2016 V shift observed for SC-Ni92. The impedance of SC-Ni92-OV was also significantly lower than that of SC-Ni92 (Figure S7). Even when charged to 4.6 V and held for 30/60 min, SC-Ni92-OV still maintained a higher capacity retention than SC-Ni92 (Figure S8). SC-Ni92-OV also exhibited better cycling performance than SC-Ni92 at a cutoff voltage of 4.4 V (Figure S9). Additionally, as shown in Figures S10 and S11, the optimal annealing temperature is 400 °C, and Ti and Mg codoping exhibits best cycling stability. It is worth noting that the cycling stability of SC-Ni92-Heat is lower than that of SC-Ni92 (Figure S12), indicating that the unanchored oxygen vacancies are detrimental to the cycling stability. To evaluate practical application potential, the samples were further tested in full cells with graphite as anodes. As presented in Figure 2f, SC-Ni92-OV displayed a capacity retention of 90.71% after 300 cycles within a voltage range of 2.65-4.5 V at 1 C in full cells, significantly higher than that of SC-Ni92 (73.49%).

Enhanced Ion and Electronic Conductivity from Oxygen Vacancies. By constructing interfacial OVs, the electrical conductivity and Li<sup>+</sup> diffusion coefficient of the single-crystal particle are significantly enhanced. As shown in Figure 3a, the electrical conductivity of SC-Ni92-OV was approximately 1.5 times higher than that of SC-Ni92 under various pressures, demonstrating that the introduction of OVs in the near-surface region of SC-Ni92-OV particles can significantly enhance the electrical conductivity. In addition,

the impedance of the entire battery system is reduced during the first cycle after using SC-Ni92-OV as a cathode (Figure S7a). To assess the Li<sup>+</sup> diffusion coefficient, galvanostatic intermittent titration technique (GITT) measurements were performed on SC-Ni92 and SC-Ni92-OV half cells (Figure 3b). SC-Ni92-OV exhibited a superior Li<sup>+</sup> diffusion coefficient and reduced polarization compared to SC-Ni92 throughout the entire delithiation/lithiation process. Furthermore, as shown in Figure S13, the Li<sup>+</sup> diffusion coefficient of SC-Ni92-Heat was like that of SC-Ni92-OV and higher than that of SC-Ni92, indicating that the OVs, rather than the permeation of Ti and Mg elements, led to the enhanced Li<sup>+</sup> diffusion ability.

To better understand the structural evolution of singlecrystal ultrahigh nickel materials during the lithiation/ delithiation process, in situ XRD measurements were performed on a self-developed cell with SC-Ni92 or SC-Ni92-OV used as the cathode, cycling at 0.33 C within 2.75-4.6 V. As shown in Figure 3c, when SC-Ni92 was charged from 2.75 to 4.1 V, the (003) peak gradually shifted to a lower angle, indicating the gradual expansion of the c-axis, likely resulting from the increasing electrostatic repulsion between adjacent oxygen layers as Li<sup>+</sup> was removed. Subsequently, the (003) peaks rapidly shifted to a higher angle, associated with the H2-H3 phase transition, 29,30 reflecting a dramatic lattice contraction along the c-axis. During the H2-H3 phase transition (Figure 3d), the pronounced phase separation suggests a nonuniform distribution of lithium ions, implying sluggish Li<sup>+</sup> diffusion kinetics in SC-Ni92.<sup>31,32</sup> It is well known that phase separation induces severe lattice strain, which is detrimental to long-term cycling performance. In contrast, the phase separation behavior was significantly suppressed in SC-Ni92-OV (Figure 3e-f), demonstrating that the interfacial

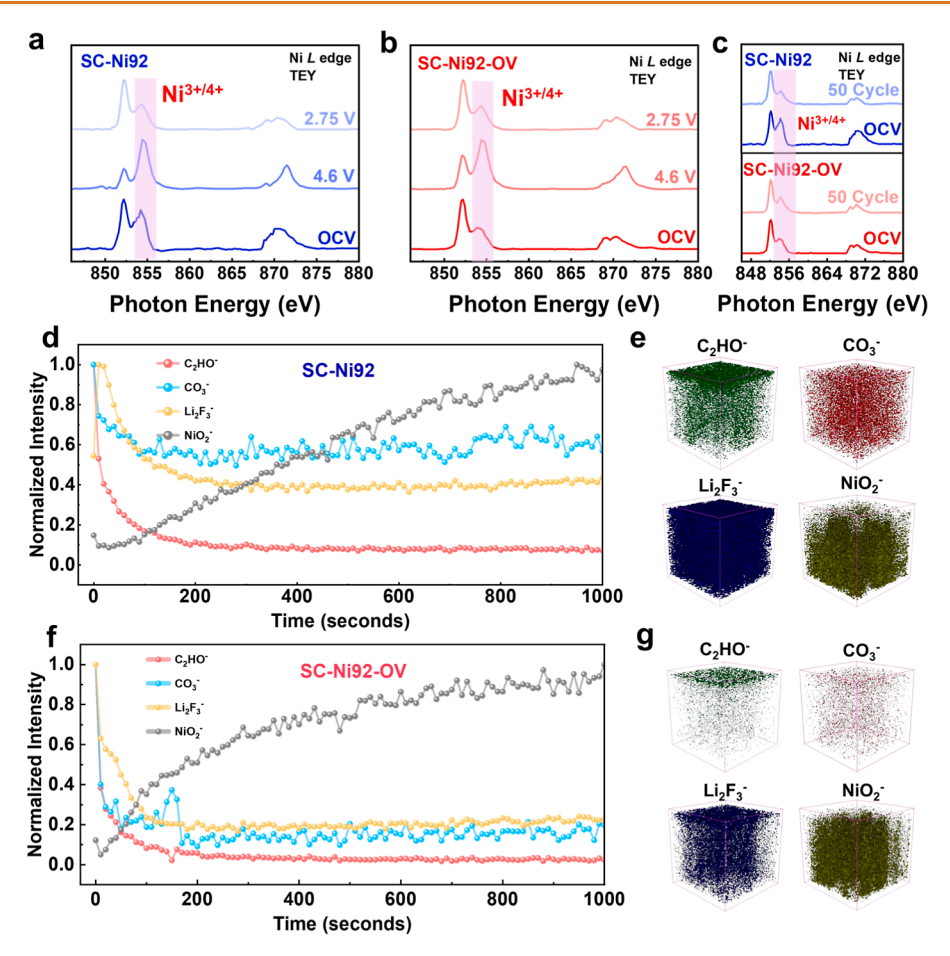


Figure 5. Ni L-edge s-XAS spectra for SC-Ni92 (a) and SC-Ni92-OV (b) at different voltage points, and comparison of the Ni L-edge s-XAS spectra at initial open-circuit voltage (OCV) and after 50 cycles for the two samples (c); TOF-SIMS depth profiles and 3D rendering of the near-surface chemical composition for  $C_2HO^-$ ,  $Li_2F_3^-$ ,  $CO_3^-$ , and  $NiO_2^-$  fragments on the surface of SC-Ni92 (d,e) and SC-Ni92-OV (f,g) cathodes

OVs greatly improve both the Li<sup>+</sup> diffusion coefficient and electrical conductivity of single-crystal ultrahigh nickel materials.

Manipulation of Oxygen Vacancies by the Pinning **Effect.** Although OVs can promote Li<sup>+</sup> and electron transport, the local environment around them is less stable and facilitates the migration of transition metals within the lattice. 12,13 During electrochemical cycling, OVs spontaneously diffuse into the bulk phase, accompanied by continuous oxygen loss at the surface. These permeated OVs can induce lattice dislocations or cracks, eventually leading to harmful phase transitions within the particles. 33,34 As shown in Figure 4a-d, we used transmission electron microscopy (TEM) to study the evolution of the intragranular structure of single-crystal particles after 200 cycles (prepared by focusing ion beam (FIB)). Dislocations (marked by green arrows) and cracks (marked by the yellow box) were clearly observed in cycled SC-Ni92 (Figure 4a). Representative high-resolution TEM images of the dislocation and crack are shown in Figures 4b-c and S14. An undesirable phase transition from a layered to a rock salt structure was observed near the crack (Figure 4c). In sharp contrast, cycled SC-Ni92-OV maintained an intact structure without forming any dislocations or cracks (Figure 4d). Statistically, SC-Ni92-OV particles exhibited fewer cracks than SC-Ni92 particles, both at high voltage states (Figures S15 and S16) and after extended cycling (Figures S17 and

S18). Furthermore, a significant difference was observed in highly delithiated electrodes after heating at 400 °C for 4 h in Ar. As shown in Figure 4e and Figure 4f, nanopores were observed within heated SC-Ni92 particles formed by the migration of OVs to the bulk. In contrast, heated SC-Ni92-OV retained an intact structure with no nanopores observed in bulk (Figure 4g and Figure 4h). In addition, Figure S19 shows O K-edge s-XAS of SC-Ni92 and SC-Ni92-OV after 50 cycles. The pre-edge peak at  $\sim$ 529 eV, attributed to transitions from the O 1s to the empty TM 3d orbitals, 35 was less intense for SC-Ni92 than SC-Ni92-OV, implying reduced Ni-O bond covalency and indicating greater oxygen loss at the SC-Ni92 surface after cycling. These results suggest that the Ti and Mg elements at the interface exert a pinning effect on OVs, inhibiting their formation and subsequent migration from the interface to the bulk. The schematic diagrams of the OVs' migration-induced degradation process are displayed in Figure 4i. The interfacial OVs were anchored by the Ti and Mg permeated layer, inhibiting migration into the bulk, due to the stronger Ti-O (662 kJ mol<sup>-1</sup>) and Mg-O (601 kJ mol<sup>-1</sup>) bonds compared to the Ni-O (391.6 kJ mol<sup>-1</sup>) and Li-O (341 kJ mol<sup>-1</sup>) bonds<sup>36-38</sup> (Figure 4j). In general, although SC-Ni92-OV initially had more interfacial OVs than SC-Ni92, the uncontrollable formation and gradual migration of OVs to the bulk was significantly suppressed during high-voltage electrochemical cycling.

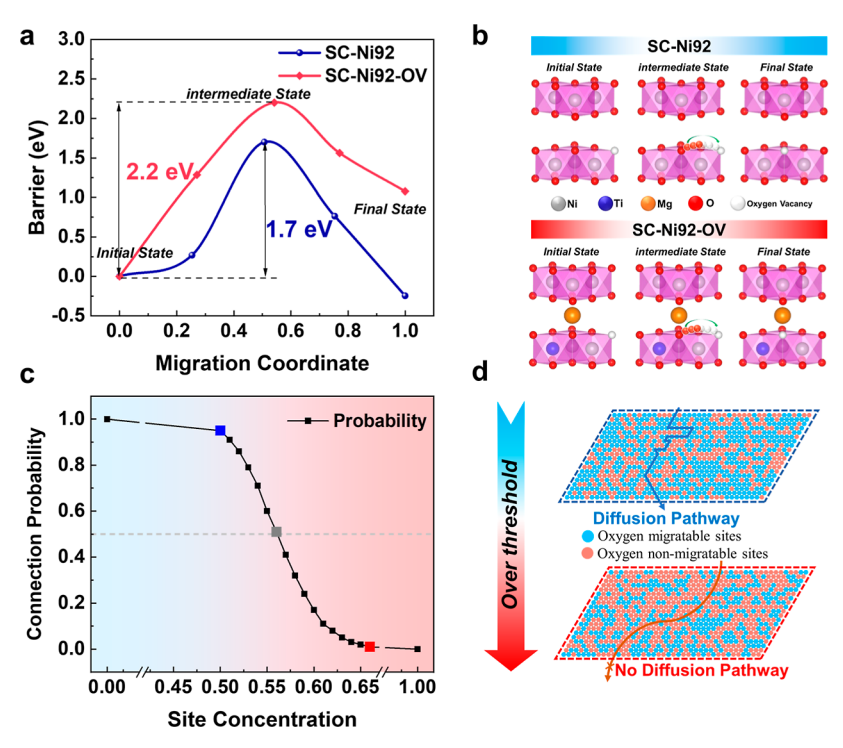


Figure 6. Calculation of the migration barrier for OVs in SC-Ni92 and SC-Ni92-OV (a); OV migration model in the Ni-O polyhedron and Ti/Mg-O polyhedron in the 87.5% delithiated state (b); simulation results of OV flow on the surface (c); comparison model of the OV seepage path after the seepage threshold (d).

The gradual migration of OVs from the surface to the bulk is accompanied by continuous oxygen evolution, which inevitably reacts with the electrolyte and causes its decomposition associated with surface Ni<sup>3+</sup> irreversible reduction. To verify this hypothesis, we performed s-XAS tests at different cycling states, XPS, and time-of-flight secondary ion mass spectrometry (TOF-SIMS) tests on cathodes subjected to 200 cycles at 1 C within 2.75-4.6 V. As shown in Figure 5a, the proportion of high-valence Ni ion (Ni3+ or Ni4+) at the interface of SC-Ni92 is significantly reduced after the first cycle, indicating that some high-valence Ni ion is reduced along with the O loss. In contrast, no significant change in the proportion of highvalence Ni ions at the interface of SC-Ni92-OV shows better redox reversibility (Figure 5b), indicating that SC-Ni92-OV is accompanied by very little O loss at the interface during the cycle. The change of high-valence Ni ion content at the interface of SC-Ni92 is more significant than SC-Ni92-OV after 50 cycles (Figure 5c). Moreover, the intensity of F-, O-, and C-containing byproducts on the surface of cycled SC-Ni92 is much higher than that of cycled SC-Ni92-OV (Figure S20). The XPS etch results indicate that the CEI of SC-Ni92 is much thicker than SC-Ni92-OV after 200 cycles (Figure S21). According to SEM images (Figures S17 and S18), the surface of cycled SC-Ni92 was much rougher than that of cycled SC-Ni92-OV, which also indicated that a thicker CEI was formed on the former. SC-Ni92 also shows a thicker rock salt surface layer (with a distorted subsurface region) than SC-Ni92-OV after 200 cycles (Figure S22). The surfaces of the cycled cathode were further analyzed by tracking changes in surface species (C<sub>2</sub>HO<sup>-</sup>, Li<sub>2</sub>F<sub>3</sub><sup>-</sup>, and CO<sub>3</sub><sup>-</sup>) by TOF-SIMS. For SC-Ni92, the normalized depth profiles of C<sub>2</sub>HO<sup>-</sup>, Li<sub>2</sub>F<sub>3</sub><sup>-</sup>, and CO<sub>3</sub><sup>-</sup> fragments stabilized at a constant value after 300 s of sputtering, demonstrating that a thick CEI had formed on its surface (Figure 5d). Correspondingly, the C<sub>2</sub>HO<sup>-</sup>, Li<sub>2</sub>F<sub>3</sub><sup>-</sup>, and

CO<sub>3</sub><sup>-</sup> fragments of SC-Ni92-OV stabilized after 200 s of sputtering (Figure 5f). The differences are visualized more clearly in the 3D models (Figure 5e,g) and chemical mappings (Figure S23). In general, the stable Ti and Mg-O octahedral surface region, constructed by Ti and Mg permeation, not only impedes the migration of OVs from the surface to the bulk but also mitigates the formation of OVs during high-voltage electrochemical cycling, thereby reducing the parasitic reactions between released oxygen and the electrolyte.

**Theoretical Calculation.** To investigate the mechanism of the pinning effect, we conducted multiscale theoretical calculations. Density functional theory (DFT) calculation (Figures S24 and S25) reveals that SC-Ni92 exhibits an OV formation energy of 0.849 eV, significantly lower than that of SC-Ni92-OV (1.734 eV) in the 87.5% delithiated state (Figure S26). This result indicates that OVs are less likely to form on the Ti/Mg-O polyhedron than on the Ni-O polyhedron. Further calculations of OV migration barriers in the 87.5% delithiated state were performed for both samples, with 1.7 and 2.2 eV obtained for SC-Ni92 and SC-Ni92-OV, respectively (Figure 6a,b). OVs encounter significant barriers when migrating from the Ni-O polyhedron to the Ti/Mg-O polyhedron, suggesting a preference for migration through an edge-shared Ni-O polyhedron. The Ti/Mg-O polyhedron thus hinders OV migration by raising the migration energy barrier. This suggests that when Ti and Mg contents reach a specific threshold, creating a corresponding concentration of bound oxygen atoms, the low-barrier percolation network of OV is fully obstructed, thereby mitigating OV migration. To further examine this mechanism, Monte Carlo simulations were performed to evaluate the probability of OV percolation<sup>39,40</sup> (Figure 6c). The simulations revealed that when the content of bound oxygen reached about 0.6 (with Ti/Mg content around 0.2, one Ti/Mg atom can bond three O atoms)

with the surface Ti-/Mg-permeated layer, the probability of forming oxygen percolation pathways sharply declined. Uniform doping of the bulk phase to block the seepage network requires a bound oxygen concentration exceeding 0.5, equivalent to approximately 17% Ti/Mg doping, which is impractical (Figure S27). As shown in Figure 6d, when the bond oxygen concentration is below the percolation threshold (with blue representing oxygen in the Ni-O polyhedron and red representing oxygen in the Ti/Mg-O polyhedron), multiple pathways for OV diffusion are present from the interface to the bulk. Upon reaching the threshold, the possibility of percolation decreases markedly from a statistical standpoint. These calculations suggest that the formation of a Ti-/Mg-rich layer on the surface of cathode single-crystal particles effectively blocks OV migration, thereby mitigating structural degradation associated with OVs.

## **CONCLUSION**

In summary, OVs were introduced in the near-surface region of single-crystal LiNi<sub>0.92</sub>Co<sub>0.06</sub>Mn<sub>0.02</sub>O<sub>2</sub> under moderately high temperatures and an oxygen atmosphere. The electrochemical performance and structural stability of ultrahigh nickel singlecrystal materials are strongly influenced by lattice OVs. The surface permeation of Ti and Mg promotes the formation of OVs during heating, while the Ti- and Mg-permeated layer suppresses the continuous formation of OVs during highvoltage cycling in return. Specifically, the preformed OVs were stabilized by the Ti- and Mg-permeated layer, which increased the formation energy and migration barrier of OVs. The stabilization of OVs leverages their benefits in enhancing conductivity and lithium-ion diffusion while mitigating their disadvantages, such as structural failure and electrolyte decomposition. As a result, oxygen vacancy-stabilized singlecrystal LiNi<sub>0.92</sub>Co<sub>0.06</sub>Mn<sub>0.02</sub>O<sub>2</sub> (SC-Ni92-OV) exhibited 86.16% capacity retention after 200 cycles at a 1 C rate within a voltage range of 2.75-4.6 V in a half-cell. Furthermore, in a 2.65-4.5 V high-voltage full-cell system with a graphite anode, SC-Ni92-OV exhibited an excellent cycling retention of 90.71% after 300 cycles, thereby advancing the commercial viability of ultrahigh nickel single crystals for high-voltage applications. This study provides a new perspective for stabilizing high-voltage stability and enhancing lithium-ion diffusion of ultrahigh nickel single crystals.

# **METHODS**

**Materials Synthesis.** Commercial high nickel single-crystal LiNi $_{0.92}$ Co $_{0.06}$ Mn $_{0.02}$ O $_2$ , 0.4 mol % nano TiO $_2$  (rutile type), and 0.8 mol % Mg(OH) $_2$  powder were heated in anhydrous ethanol (35 °C) and stirred evenly at the stirring speed (500 rpm) until the ethanol was completely volatilized. Then, the mixture was dried in a vacuum oven at 105 °C for 7 h. Afterward, the well-homogenized powder was heated at 400 °C for 5 h in a tube furnace under an oxygen atmosphere (O $_2 \ge 99.5$ %) and then cooled down naturally, resulting in the final sample labeled as SC-Ni92-OV. For comparison, the single-crystal LiNi $_{0.92}$ Co $_{0.06}$ Mn $_{0.02}$ O $_2$  was heated at the same conditions and the final products were labeled as SC-Ni92-Heat.

Materials Characterizations. The crystal structure was examined by X-ray diffraction (XRD, D8 Discover, Bruker, Germany) and the corresponding crystal refinement was conducted on GSASII software. The in situ XRD characterization was carried out with the assistance of a special cell (Beijing Science Star Technology Co., China). The transmission electron microscopy (TEM) characterization was acquired on a field-emission transmission electron microscope (JEOL-3200FS, Japan) with an accelerating voltage of 300 kV. The

scanning electron microscope (SEM, Zeiss-SUPRA-55, Germany) coupled to the X-Max EDS detector was used to investigate the morphologies and elemental distribution of the samples. The content of the elements in the sample was determined by inductively coupled plasma-mass spectrometry (ICP-OES, PE/Avio 220 Max, PerkinElmer, USA). The electron paramagnetic resonance (EPR, A300-10, Bruker, Germany) was employed to qualitatively analyze the oxygen vacancies. The Ni L-edge and O K-edge soft X-ray absorption spectroscopy (sXAS) spectra were acquired at the Shanghai Synchrotron Radiation Facility (Shanghai, China). The surface chemistry was analyzed by X-ray Photoelectron Spectroscopy (XPS, ESCAlab 250Xi, Thermo Fisher, USA) with Al K $\alpha$  radiation. The time-of-flight secondary-ion mass spectrometry (TOF-SIMS, ULVAC-PHI nanoTOF II, Japan) was used to investigate the surface of the cycled cathodes. The large cross-section of particles is prepared by a focused ion beam (FIB, Leica EM TIC 3X, Germany). The active materials were pressed into discs under different pressures for the electronic conductivity measurements. The formula to calculate the conductivity is  $\delta = L/(SR)$ , wherein R, L, and S are the resistance, thickness, and cross-sectional area of the discs, respectively.

**Electrochemical Measurements.** To fabricate the electrode, 80 wt % active material, 10 wt % PVDF dissolved into N-Methyl-2-Pyrrolidinone (NMP), and 10 wt % conductive carbon were mixed for 30 min in a homogenizer, followed by coating the slurry onto the aluminum foil with the help of a blade and dried at 105 °C for 12 h in a vacuum oven. The mass loading in the cathode films was  $\sim$ 5 mg cm $^{-2}$ . The CR2032 coin cells were assembled in a glovebox (MIKROUNA) filled with argon. In the coin cells, 1 M LiPF<sub>6</sub> dissolved in ethylene/diethyl carbonate at a volume rate 3:7 as the electrolyte, Li-foil or prelithiated graphite as the counter electrode, and Celgard 2316 as the separator. The half cells were tested in the voltage range of 2.75–4.6 V. The full cells were tested in the voltage range of 2.65–4.5 V. The galvanostatic charge/discharge and galvanostatic intermittent titration technique tests were performed using the Neware testing system.

Calculation Methods. DFT Calculations. Spin-polarized density functional theory (DFT) calculations were conducted using the VASP code<sup>41-43</sup> based on the projector-augmented wave (PAW) method. The exchange correlation potential was described using the generalized gradient approximation (GGA) with the Perdew-Burke-Ernzerhof (PBE) functional. The plane-wave cutoff energy and the convergence criterion for electronic energy were set at  $5\overline{20}$  eV and  $10^{-5}$  eV, respectively. Gamma-centered Monkhorst-Pack k-point grid sampling was employed for the Brillouin zone, with a density of at least 1000 (the number of atoms per cell) in all calculations. The geometries were fully relaxed, until the forces acting on the atoms were less than 0.02 eV/Å. To accurately characterize the strong correlation of transition-metal d-electrons, the GGA + U method was employed in the calculations 47,48 with the Hubbard U parameters set at 6.2, 3.3, 3.9, and 4.2 eV for Ni, Co, Mn, and Ti, respectively. 49-51 The magnetic order of the transition metals was set to ferromagnetic. The migration barriers of oxygen vacancies were calculated using the climbing image nudged elastic band (CI-NEB) method,<sup>48</sup> and the pathways were optimized until the maximum force was less than 0.03 eV/Å. To examine the influences on the thermodynamic stability of lattice oxygen and Li-ion diffusion barriers, we constructed supercells containing 32 LiMO2 formulas and calculations at nearly fully delithiated states (e.g., Li<sub>4</sub>Ni<sub>29</sub>Co<sub>2</sub>MnO<sub>64</sub> for SC-Ni92 and Li<sub>2</sub>MgNi<sub>28</sub>Co<sub>2</sub>MnO<sub>64</sub> for SC-Ni92-OV). One oxygen vacancy was introduced into the supercells, and one Ni was replaced by Ti and with one Mg included in the Li layer to estimate the model of Ti and Mg near-surface doping, respectively. Li ions were placed as far from the oxygen vacancy as possible to eliminate their interference with the calculation of migration energy barriers. When Mg was introduced, Li ions were partially removed to ensure a charge balance.

The formation energy of the oxygen vacancy is defined as

$$V_{\mathrm{O}} = E(\mathrm{Li}_{x}\mathrm{M}_{y}\mathrm{O}_{2-\delta}) + \frac{\delta}{2}E(\mathrm{O}_{2}) - E(\mathrm{Li}_{x}\mathrm{M}_{y}\mathrm{O}_{2})$$

where  $E(\text{Li}_x M_y O_{2-\delta})$  and  $E(\text{Li}_x M_y O_2)$  are the internal energies of the supercell with and without the oxygen vacancy, respectively.  $E(O_2)$  is the internal energy of the oxygen. A -1.36 eV energy correction for the  $O_2$  molecule was obtained to account for self-interaction errors in the GGA calculations.  $^{43}$ 

**Monte Carlo (MC) Simulations.** MC simulations were performed to investigate the percolation probability of oxygen vacancies in the network. In the MC simulations, a two-dimensional (2D) honeycomb network grid was established to represent the simplified oxygen percolation network. The dimensions of the network grid were established as  $100 \times 100$  for the bulk and  $60 \times 20$  for the surface permeation layer. The percolation probability of the surface permeation layer was defined as the probability of connectivity between the top and bottom edges of the grid. The number of simulations was established at a minimum of 10,000 to minimize the effects of randomness on the statistical probability.

## **ASSOCIATED CONTENT**

## **Data Availability Statement**

All relevant data that support the findings of this study are presented in the manuscript and Supporting Information file. Source data are available from the corresponding author upon reasonable request.

# **Supporting Information**

The Supporting Information is available free of charge at https://pubs.acs.org/doi/10.1021/acsnano.5c05412.

Characterizations of the cathode materials such as SEM, EDS, TEM, XRD, XPS, ICP-OES, sXAS, and TOF-SIMS; electrochemical characterizations such as cycle performance, EIS, and GITT; and DFT calculations of oxygen vacancy formation energy and simulation results of oxygen vacancy flow on the surface and bulk (PDF)

## **AUTHOR INFORMATION**

# **Corresponding Authors**

Feng Pan — School of Advanced Materials, Peking University Shenzhen Graduate School, Shenzhen 518055, China; orcid.org/0000-0002-8216-1339; Email: panfeng@pkusz.edu.cn

Xinghua Tan — School of Advanced Materials, Peking University Shenzhen Graduate School, Shenzhen 518055, China; Shenyang National Laboratory for Materials Science, Institute of Metal Research, Chinese Academy of Sciences, Shenyang 110016, China; Email: xhtan@imr.ac.cn

#### **Authors**

Yongzhi Liang — School of Advanced Materials, Peking University Shenzhen Graduate School, Shenzhen 518055, China

Haoyu Xue – School of Advanced Materials, Peking University Shenzhen Graduate School, Shenzhen 518055, China

Minzhi Zhan — School of Advanced Materials, Peking University Shenzhen Graduate School, Shenzhen 518055, China

Hongbin Cao – School of Advanced Materials, Peking University Shenzhen Graduate School, Shenzhen 518055, China

Zhongxing Xu — School of Advanced Materials, Peking University Shenzhen Graduate School, Shenzhen 518055, China

Xinghan Chen – School of Advanced Materials, Peking University Shenzhen Graduate School, Shenzhen 518055, China

Jiajie Liu – School of Advanced Materials, Peking University Shenzhen Graduate School, Shenzhen 518055, China

Shunning Li — School of Advanced Materials, Peking University Shenzhen Graduate School, Shenzhen 518055, China; orcid.org/0000-0002-5381-6025

Complete contact information is available at: https://pubs.acs.org/10.1021/acsnano.5c05412

## **Author Contributions**

Y.L., H.X., and M.Z. contributed equally to this work.

#### **Notes**

The authors declare no competing financial interest.

## **ACKNOWLEDGMENTS**

This work was financially supported by the Basic and Applied Basic Research Foundation of Guangdong Province (No. 2023A1F515111131), the National Natural Science Foundation of China (No. 92472206), the Major Science and Technology Infrastructure Project of Material Genome Big-Science Facilities Platform supported by Municipal Development and Reform Commission of Shenzhen, International joint Research Center for Electric Vehicle Power Battery and Materials (No. 2015B01015), Guangdong Key Laboratory of Design and calculation of New Energy Materials (No. 2017B030301013), Shenzhen Key Laboratory of New Energy Resources Genome Preparation and Testing (No. ZDSYS201707281026184), and Liaoning Provincial Science Fund for Distinguished Young Scholar (No. 2024JH3/ 50100017).

# **ABBREVIATIONS**

SC-Ni92, pristine single-crystal LiNi $_{0.92}$ Co $_{0.06}$ Mn $_{0.02}$ O $_2$ ; SC-Ni92-Heat, LiNi $_{0.92}$ Co $_{0.06}$ Mn $_{0.02}$ O $_2$  heated in an oxygen atmosphere; SC-Ni92-OV, oxygen vacancy-anchored single-crystal LiNi $_{0.92}$ Co $_{0.06}$ Mn $_{0.02}$ O $_2$ ; CEI, cathode electrolyte interphase

## **REFERENCES**

- (1) Zhang, R.; Wang, C.; Zou, P.; Lin, R.; Ma, L.; Yin, L.; Li, T.; Xu, W.; Jia, H.; Li, Q.; Sainio, S.; Kisslinger, K.; Trask, S. E.; Ehrlich, S. N.; Yang, Y.; Kiss, A. M.; Ge, M.; Polzin, B. J.; Lee, S. J.; Xu, W.; Ren, Y.; Xin, H. L. Compositionally complex doping for zero-strain zero-cobalt layered cathodes. *Nature* **2022**, *610* (7930), *67*—73.
- (2) Cano, Z. P.; Banham, D.; Ye, S.; Hintennach, A.; Lu, J.; Fowler, M.; Chen, Z. Batteries and fuel cells for emerging electric vehicle markets. *Nat. Energy* **2018**, *3* (4), 279–289.
- (3) Liu, T.; Yu, L.; Liu, J.; Dai, A.; Zhou, T.; Wang, J.; Huang, W.; Li, L.; Li, M.; Li, T.; Huang, X.; Xiao, X.; Ge, M.; Ma, L.; Zhuo, Z.; Amine, R.; Chu, Y. S.; Lee, W.-K.; Wen, J.; Amine, K. Ultrastable cathodes enabled by compositional and structural dual-gradient design. *Nat. Energy* **2024**, *9* (10), 1252–1263.
- (4) Liu, W.; Li, D.; Liu, Y.; Luo, D.; Xu, R. A Critical Review of Single-Crystal LiNixMn yCo1-x-yO2 Cathode Materials. *Renewables* **2024**, 2 (1), 25–51.
- (5) Xu, Z.; Chen, X.; Fan, W.; Zhan, M.; Mu, X.; Cao, H.; Wang, X.; Xue, H.; Gao, Z.; Liang, Y.; Liu, J.; Tan, X.; Pan, F. High-Entropy Rock-Salt Surface Layer Stabilizes the Ultrahigh-Ni Single-Crystal Cathode. *ACS Nano* **2024**, *18* (49), 33706–33717.
- (6) Xue, H.; Liang, Y.; Huang, Y.; Ji, Y.; Xu, Z.; Chen, X.; Wang, H.; Liu, J.; Amine, K.; Liu, T.; Tan, X.; Pan, F. In Situ Conversion of

- Artificial Proton-Rich Shell to Inorganic Maskant Toward Stable Single-Crystal Ni-Rich Cathode. Adv. Mater. 2025, 37 (7), 2415860.
- (7) Wang, C.; Han, L.; Zhang, R.; Cheng, H.; Mu, L.; Kisslinger, K.; Zou, P.; Ren, Y.; Cao, P.; Lin, F.; Xin, H. L. Resolving atomic-scale phase transformation and oxygen loss mechanism in ultrahigh-nickel layered cathodes for cobalt-free lithium-ion batteries. *Matter* **2021**, *4* (6), 2013–2026.
- (8) Yan, P.; Zheng, J.; Gu, M.; Xiao, J.; Zhang, J.-G.; Wang, C.-M. Intragranular cracking as a critical barrier for high-voltage usage of layer-structured cathode for lithium-ion batteries. *Nat. Commun.* **2017**, *8* (1), 14101.
- (9) Zhang, R.; Wang, C.; Zou, P.; Lin, R.; Ma, L.; Li, T.; Hwang, I.-h.; Xu, W.; Sun, C.; Trask, S.; Xin, H. L. Long-life lithium-ion batteries realized by low-Ni, Co-free cathode chemistry. *Nat. Energy* **2023**, *8* (7), 695–702.
- (10) Zhang, H.; May, B. M.; Omenya, F.; Whittingham, M. S.; Cabana, J.; Zhou, G. Layered Oxide Cathodes for Li-Ion Batteries: Oxygen Loss and Vacancy Evolution. *Chem. Mater.* **2019**, *31* (18), 7790–7798.
- (11) Wang, C.; Zhang, R.; Siu, C.; Ge, M.; Kisslinger, K.; Shin, Y.; Xin, H. L. Chemomechanically Stable Ultrahigh-Ni Single-Crystalline Cathodes with Improved Oxygen Retention and Delayed Phase Degradations. *Nano Lett.* **2021**, 21 (22), 9797–9804.
- (12) Lee, S.; Jin, W.; Kim, S. H.; Joo, S. H.; Nam, G.; Oh, P.; Kim, Y.-K.; Kwak, S. K.; Cho, J. Oxygen Vacancy Diffusion and Condensation in Lithium-Ion Battery Cathode Materials. *Angew. Chem., Int. Ed.* **2019**, *58* (31), 10478–10485.
- (13) Meng, X.-H.; Lin, T.; Mao, H.; Shi, J.-L.; Sheng, H.; Zou, Y.-G.; Fan, M.; Jiang, K.; Xiao, R.-J.; Xiao, D.; Gu, L.; Wan, L.-J.; Guo, Y.-G. Kinetic Origin of Planar Gliding in Single-Crystalline Ni-Rich Cathodes. J. Am. Chem. Soc. 2022, 144 (25), 11338–11347.
- (14) Wu, C.; Wu, Y.; Yang, X.; Xin, T.; Chen, S.; Yang, M.; Peng, Y.; Xu, H.; Yin, Y.; Deng, T.; Feng, X. Thermal Runaway Suppression of High-Energy Lithium-Ion Batteries by Designing the Stable Interphase. J. Electrochem. Soc. 2021, 168 (9), 090563.
- (15) Qiu, B.; Zhang, M.; Wu, L.; Wang, J.; Xia, Y.; Qian, D.; Liu, H.; Hy, S.; Chen, Y.; An, K.; Zhu, Y.; Liu, Z.; Meng, Y. S. Gas—solid interfacial modification of oxygen activity in layered oxide cathodes for lithium-ion batteries. *Nat. Commun.* **2016**, *7* (1), 12108.
- (16) Jin, J.; Liu, Y.; Zhao, X.; Liu, H.; Deng, S.; Shen, Q.; Hou, Y.; Qi, H.; Xing, X.; Jiao, L.; Chen, J. Annealing in Argon Universally Upgrades the Na-Storage Performance of Mn-Based Layered Oxide Cathodes by Creating Bulk Oxygen Vacancies. *Angew. Chem., Int. Ed.* **2023**, *62* (15), No. e202219230.
- (17) Kim, H.-S.; Cook, J. B.; Lin, H.; Ko, J.; Tolbert, S.; Ozolins, V.; Dunn, B. Oxygen vacancies enhance pseudocapacitive charge storage properties of MoO3–x. *Nat. Mater.* **2017**, *16* (4), 454–460.
- (18) Wang, K.; Wang, Y.; Yang, B.; Li, Z.; Qin, X.; Zhang, Q.; Lei, L.; Qiu, M.; Wu, G.; Hou, Y. Highly active ruthenium sites stabilized by modulating electron-feeding for sustainable acidic oxygenevolution electrocatalysis. *Energy Environ. Sci.* **2022**, *15* (6), 2356–2365.
- (19) Tian, Y.; Liu, X.; Xu, L.; Yuan, D.; Dou, Y.; Qiu, J.; Li, H.; Ma, J.; Wang, Y.; Su, D.; Zhang, S. Engineering Crystallinity and Oxygen Vacancies of Co(II) Oxide Nanosheets for High Performance and Robust Rechargeable Zn—Air Batteries. *Adv. Funct. Mater.* **2021**, *31* (20), 2101239.
- (20) Amriou, T.; Khelifa, B.; Aourag, H.; Aouadi, S. M.; Mathieu, C. Ab initio investigation of the Jahn-Teller distortion effect on the stabilizing lithium intercalated compounds. *Mater. Chem. Phys.* **2005**, 92 (2), 499–504.
- (21) Genreith-Schriever, A. R.; Banerjee, H.; Menon, A. S.; Bassey, E. N.; Piper, L. F. J.; Grey, C. P.; Morris, A. J. Oxygen hole formation controls stability in LiNiO2 cathodes. *Joule* 2023, 7 (7), 1623–1640. (22) Hou, X.-Y.; Kimura, Y.; Tamenori, Y.; Nitta, K.; Yamagishi, H.; Amezawa, K.; Nakamura, T. Thermodynamic Analysis Enables Quantitative Evaluation of Lattice Oxygen Stability in Li-Ion Battery Cathodes. *ACS Energy Lett.* 2022, 7 (5), 1687–1693.

- (23) Chen, J.; Yang, Y.; Tang, Y.; Wang, Y.; Li, H.; Xiao, X.; Wang, S.; Darma, M. S. D.; Etter, M.; Missyul, A.; Tayal, A.; Knapp, M.; Ehrenberg, H.; Indris, S.; Hua, W. Constructing a Thin Disordered Self-Protective Layer on the LiNiO2 Primary Particles Against Oxygen Release. *Adv. Funct. Mater.* **2023**, 33 (6), 2211515.
- (24) Zhang, W.; Cai, L.; Cao, S.; Qiao, L.; Zeng, Y.; Zhu, Z.; Lv, Z.; Xia, H.; Zhong, L.; Zhang, H.; Ge, X.; Wei, J.; Xi, S.; Du, Y.; Li, S.; Chen, X. Interfacial Lattice-Strain-Driven Generation of Oxygen Vacancies in an Aerobic-Annealed TiO2(B) Electrode. *Adv. Mater.* 2019, 31 (52), 1906156.
- (25) Zhang, N.; Li, X.; Ye, H.; Chen, S.; Ju, H.; Liu, D.; Lin, Y.; Ye, W.; Wang, C.; Xu, Q.; Zhu, J.; Song, L.; Jiang, J.; Xiong, Y. Oxide Defect Engineering Enables to Couple Solar Energy into Oxygen Activation. J. Am. Chem. Soc. 2016, 138 (28), 8928–8935.
- (26) Foo, C.; Li, Y.; Lebedev, K.; Chen, T.; Day, S.; Tang, C.; Tsang, S. C. E. Characterisation of oxygen defects and nitrogen impurities in TiO2 photocatalysts using variable-temperature X-ray powder diffraction. *Nat. Commun.* **2021**, *12* (1), 661.
- (27) Lin, R.; Bak, S.-M.; Shin, Y.; Zhang, R.; Wang, C.; Kisslinger, K.; Ge, M.; Huang, X.; Shadike, Z.; Pattammattel, A.; Yan, H.; Chu, Y.; Wu, J.; Yang, W.; Whittingham, M. S.; Xin, H. L.; Yang, X.-Q. Hierarchical nickel valence gradient stabilizes high-nickel content layered cathode materials. *Nat. Commun.* **2021**, *12* (1), 2350.
- (28) Blume, R.; Calvet, W.; Ghafari, A.; Mayer, T.; Knop-Gericke, A.; Schlögl, R. Structural and Chemical Properties of NiOx Thin Films: Oxygen Vacancy Formation in O2 Atmosphere. *ChemPhysChem* **2023**, 24 (23), No. e202300231.
- (29) Liu, T.; Yu, L.; Lu, J.; Zhou, T.; Huang, X.; Cai, Z.; Dai, A.; Gim, J.; Ren, Y.; Xiao, X.; Holt, M. V.; Chu, Y. S.; Arslan, I.; Wen, J.; Amine, K. Rational design of mechanically robust Ni-rich cathode materials via concentration gradient strategy. *Nat. Commun.* 2021, 12 (1), 6024.
- (30) Liang, C.; Jiang, L.; Wei, Z.; Zhang, W.; Wang, Q.; Sun, J. Insight into the structural evolution and thermal behavior of LiNi0.8Co0.1Mn0.1O2 cathode under deep charge. *J. Energy Chem.* **2022**, *65*, 424–432.
- (31) Ryu, H.-H.; Namkoong, B.; Kim, J.-H.; Belharouak, I.; Yoon, C. S.; Sun, Y.-K. Capacity Fading Mechanisms in Ni-Rich Single-Crystal NCM Cathodes. *ACS Energy Lett.* **2021**, *6* (8), 2726–2734.
- (32) Park, N.-Y.; Park, G.-T.; Kim, S.-B.; Jung, W.; Park, B.-C.; Sun, Y.-K. Degradation Mechanism of Ni-Rich Cathode Materials: Focusing on Particle Interior. *ACS Energy Lett.* **2022**, *7* (7), 2362–2369.
- (33) Ahmed, S.; Pokle, A.; Schweidler, S.; Beyer, A.; Bianchini, M.; Walther, F.; Mazilkin, A.; Hartmann, P.; Brezesinski, T.; Janek, J.; Volz, K. The Role of Intragranular Nanopores in Capacity Fade of Nickel-Rich Layered Li(Ni1-x-yCoxMny)O2 Cathode Materials. *ACS Nano* **2019**, *13* (9), 10694–10704.
- (34) Zhang, H.; Omenya, F.; Yan, P.; Luo, L.; Whittingham, M. S.; Wang, C.; Zhou, G. Rock-Salt Growth-Induced (003) Cracking in a Layered Positive Electrode for Li-Ion Batteries. *ACS Energy Lett.* **2017**, *2* (11), 2607–2615.
- (35) Li, B.; Yan, H.; Ma, J.; Yu, P.; Xia, D.; Huang, W.; Chu, W.; Wu, Z. Manipulating the Electronic Structure of Li-Rich Manganese-Based Oxide Using Polyanions: Towards Better Electrochemical Performance. *Adv. Funct. Mater.* **2014**, 24 (32), 5112–5118.
- (36) He, J.; Li, Y.; Luo, W.; Cao, Y.; Zhao, C.; Dong, P.; Duan, J.; Wang, D.; Wang, X.; Zhou, Z.; Zhang, Y. Enhanced reversibility of single crystal Ni-rich cathode materials via Ti doping. *Electrochim. Acta* 2024, 479, 143855.
- (37) Li, H.; Zhu, Y.; Ye, Q.; Hu, W.; Zhou, Q. First-principle study on the geometric and electronic structure of Mg-doped LiNiO2 for Li-ion batteries. *J. Mol. Model.* **2023**, *29* (12), 389.
- (38) Tong, Q.; Yang, Y.; Shi, J.; Yan, J.; Zheng, L. Synthesis and Storage Performance of the Doped LiMn2O4 Spinel. *J. Electrochem. Soc.* 2007, 154 (7), A656.
- (39) Newman, M. E. J.; Ziff, R. M. Efficient Monte Carlo Algorithm and High-Precision Results for Percolation. *Phys. Rev. Lett.* **2000**, 85 (19), 4104–4107.

- (40) Chen, Z.; Zhang, W.; Liu, J.; Zhang, M.; Li, S.; Pan, F. Influence of Li Content on the Topological Inhibition of Oxygen Loss in Li-Rich Cathode Materials. *Adv. Mater.* **2024**, *36* (27), 2403307.
- (41) Kresse, G.; Hafner, J. Ab initio molecular dynamics for liquid metals. *Phys. Rev. B: Condens. Matter Mater. Phys.* **1993**, 47 (1), 558–561.
- (42) Kresse, G.; Furthmüller, J. Efficient iterative schemes for ab initio total-energy calculations using a plane-wave basis set. *Phys. Rev. B: Condens. Matter Mater. Phys.* **1996**, *54* (16), 11169–11186.
- (43) Mishra, S. K.; Ceder, G. Structural stability of lithium manganese oxides. *Phys. Rev. B: Condens. Matter Mater. Phys.* **1999**, 59 (9), 6120–6130.
- (44) Blöchl, P. E. Projector augmented-wave method. *Phys. Rev. B: Condens. Matter Mater. Phys.* **1994**, 50 (24), 17953–17979.
- (45) Kresse, G.; Joubert, D. From ultrasoft pseudopotentials to the projector augmented-wave method. *Phys. Rev. B: Condens. Matter Mater. Phys.* **1999**, *59* (3), 1758–1775.
- (46) Perdew, J. P.; Burke, K.; Ernzerhof, M. Generalized Gradient Approximation Made Simple. *Phys. Rev. Lett.* **1996**, 77 (18), 3865–3868
- (47) Dudarev, S. L.; Botton, G. A.; Savrasov, S. Y.; Humphreys, C. J.; Sutton, A. P. Electron-energy-loss spectra and the structural stability of nickel oxide: An LSDA+U study. *Phys. Rev. B: Condens. Matter Mater. Phys.* 1998, 57 (3), 1505–1509.
- (48) Anisimov, V. I.; Zaanen, J.; Andersen, O. K. Band theory and Mott insulators: Hubbard U instead of Stoner I. *Phys. Rev. B: Condens. Matter Mater. Phys.* **1991**, 44 (3), 943–954.
- (49) Wang, L.; Maxisch, T.; Ceder, G. Oxidation energies of transition metal oxides within the GGA+U framework. *Phys. Rev. B: Condens. Matter Mater. Phys.* **2006**, 73 (19), 195107.
- (50) Liu, M.; Rong, Z.; Malik, R.; Canepa, P.; Jain, A.; Ceder, G.; Persson, K. A. Spinel compounds as multivalent battery cathodes: a systematic evaluation based on ab initio calculations. *Energy Environ. Sci.* **2015**, *8* (3), 964–974.
- (51) Kong, F.; Longo, R. C.; Park, M.-S.; Yoon, J.; Yeon, D.-H.; Park, J.-H.; Wang, W.-H.; Kc, S.; Doo, S.-G.; Cho, K. Ab initio study of doping effects on LiMnO2 and Li2MnO3 cathode materials for Li-ion batteries. *J. Mater. Chem. A* **2015**, 3 (16), 8489–8500.

